HHS Public Access

Author manuscript

J Am Chem Soc. Author manuscript; available in PMC 2023 September 14.

Published in final edited form as:

J Am Chem Soc. 2022 September 14; 144(36): 16553–16558. doi:10.1021/jacs.2c06231.

Dual Hydrazine Equipped Turn-On Manganese-Based Probes for Magnetic Resonance Imaging of Liver Fibrogenesis

Yingying Ning[1], **Iris Y. Zhou**[1], **Nicholas J. Rotile**[1], **Pamela Pantazopoulos**[1], **Huan Wang**[1], **Stephen Cole Barrett**[2], **Mozhdeh Sojoodi**[2], **Kenneth K. Tanabe**[2], **Peter Caravan**[1,*]

[1]Athinoula A. Martinos Center for Biomedical Imaging, Institute for Innovation in Imaging, Department of Radiology, Massachusetts General Hospital, Harvard Medical School, Boston, MA 02129, USA

[2]Division of Gastrointestinal and Oncologic Surgery, Massachusetts General Hospital, Harvard Medical School, Boston, MA 02114, USA

Abstract

Liver fibrogenesis is accompanied by upregulation of lysyl oxidase enzymes which catalyze oxidation of lysine ε-amino groups on extracellular matrix proteins to form the aldehyde containing amino acid allysine (Lys^{Ald}). Here, we describe the design and synthesis of novel manganese-based MRI probes with high signal amplification for imaging liver fibrogenesis. Rational design of a series of stable hydrazine equipped manganese MRI probes gives **Mn-2CHyd** with the highest affinity and turn-on relaxivity (4-fold) upon reaction with Lys^{Ald}. Dynamic PET-MRI study using [^{52}**Mn]Mn-2CHyd** showed low liver uptake of the probe in healthy mice. The ability of the probe to detect liver fibrogenesis was then demonstrated *in vivo* in CCl_4 injured mice. This study enables further development and application of manganese-based hydrazine equipped probes for imaging liver fibrogenesis.

Graphical Abstract

*Corresponding Author: Peter Caravan. pcaravan@mgh.harvard.edu.

Author Contributions:

All authors have contributed to the design and implementation of the studies reported here and have given approval to the final version of the manuscript.

Supporting Information

Detailed synthesis and characterization data, additional experimental details, materials, and methods. These materials are available free of charge via the Internet at http://pubs.acs.org.

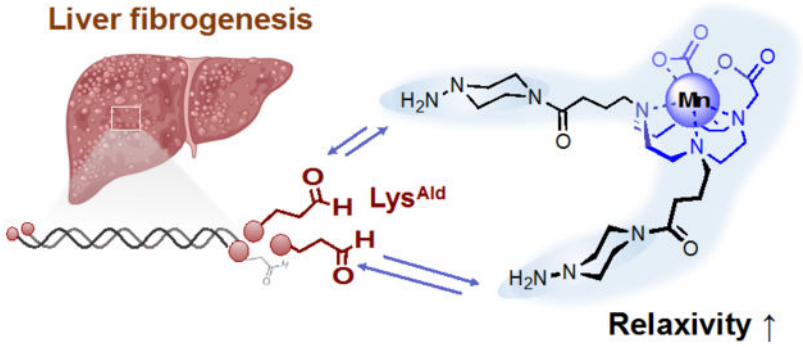

Keywords

aldehyde; lysyl oxidase; allysine; PET

INTRODUCTION

Liver fibrosis is a major cause of morbidity and mortality in liver diseases due to chronic inflammation arising from viral hepatitis B or C infection, autoimmune and biliary diseases, alcoholic and nonalcoholic steatohepatitis, etc.[1, 2] Fibrosis is characterized by the progressive accumulation of extracellular matrix (ECM) components in liver and has high potential to progress into cirrhosis, hepatocellular carcinoma, liver failure, and/or death, making it a great economic and societal burden.[3] Moreover, advanced fibrosis is classically considered irreversible and the only curative treatment for end stage cirrhosis is transplantation, highlighting the need for early detection. Biopsy is the clinical gold standard for accessing the onset of liver fibrosis and its disease activity, i.e. fibrogenesis, and for pathologically staging the severity of liver fibrosis, but biopsy is invasive, suffers sampling error, and has complication risk.[4] The lack of non-invasive methods to detect and quantify liver fibrogenesis greatly hampers the diagnosis of liver fibrosis and hampers development of new therapies.

In liver fibrogenesis, chronic liver damage leads to the activation and proliferation of hepatic stellate cells which remodel ECM.[1, 2] Upregulation of the lysyl oxidase (LOX) family of enzymes catalyze oxidation of lysine ε-amino groups on ECM (chiefly collagen) to form aldehyde allysine (Lys^{Ald}) which then undergoes cross-linking reactions with other proteins to stabilize the fibrotic ECM (Figure 1). Our group has demonstrated that Lys^{Ald} is a biomarker of fibrogenesis and that gadolinium-based magnetic resonance (MR) probes functionalized with hydrazine moiety can covalently bind to Lys^{Ald} *in vivo* to robustly stage and quantify fibrogenesis.[5, 6] However, there is concern about the long-term safety of Gd-based contrast agents.[7] Gadolinium is associated with nephrogenic systemic fibrosis, a potentially lethal disorder with scleroderma-like skin lesions that occurs in patients with reduced kidney function.

Manganese complexes are promising alternatives for Gd^{3+} complexes as MRI contrast agents.[8] High spin Mn(II) complexes have a high spin quantum number S = 5/2, long

electronic relaxation times, and fast water exchange of coordinated water ligands (>10^6 s^{-1}), which together result in potent relaxation of water protons. Manganese is also an essential element in the human body and small amounts of retained manganese may be processed and cleared *via* endogenous mechanisms. Moreover, Mn has a positron emission tomography (PET) isotope ^{52}Mn with the half-life of 5.6 day, allowing the assessment of whole-body pharmacokinetics over a period of days using PET-MRI.[9] However, Mn(II) complexes are in general labile due to the absence of ligand field stabilization energy,[10] and only limited examples of Mn(II) complexes with high thermodynamic and kinetic stability have been reported so far.[11–13] This is a particular challenge for imaging pathology in the liver since free Mn^{2+} is avidly taken up by hepatocytes in normal liver and would lead to a high background signal. Design of responsive and targeted manganese contrast agents is much more challenging.[14, 15]

A manganese-based MR probe for imaging liver fibrogenesis must meet several requirements: 1) low relaxivity when not bound to Lys^{Ald} to minimize background signal; 2) high relaxivity when bound to Lys^{Ald} to increase signal at site of fibrosis; 3) high kinetic inertness to prevent release of free Mn^{2+} which would lead to high liver background signal; 4) minimal hepatobiliary elimination of the intact complex to minimize liver background; 5) redox stable Mn^{2+} complex, as Mn^{3+} can oxidize hydrazine.[16] Based on these design requirements, here we synthesize novel hydrazine equipped manganese-based MRI probes for detection of liver fibrogenesis.

RESULTS AND DISCUSSION

Probe design and synthesis

We designed dual binding manganese probes based on ***cis*-Mn-1,4-DO2A** (Figure 2a) which was shown to be stable against oxidation, has high thermodynamic stability and kinetic inertness, and an average of 0.9 water molecules in the inner coordination sphere (*q*).[17, 18] We used a dual binder approach to increase the reaction on-rate with Lys^{Ald} and to provide a large turn-on in relaxivity upon binding, as the “dual locked” probe will reduce internal motion of the protein-bound Mn complex.[19, 20] Accordingly, two piperazino-hydrazine or hydrazide moieties were introduced in the skeleton of ***cis*-Mn-1,4-DO2A**, to form the Mn(II) complexes **Mn-2CHyd** and **Mn-2Hyd** respectively. The piperazino-hydrazine moiety was shown to have higher reactivity and affinity for Lys^{Ald} compared to an analogous hydrazide.[21] **Mn-2CHyd** and **Mn-2Hyd** were synthesized in 5 steps from cyclen-1,4-*t*-Bu-diacetic acid. **Mn-1CHyd**, which possess one piperazino-hydrazine, was synthesized as a control. Detailed synthetic procedures and characterizations can be found in the supporting information (Figure S1–25).

In vitro characterization

Cyclic voltammetry of **Mn-1,4-DO2A** in H_2O (Figure 2b) displays a quasi-reversible Mn^{II}/Mn^{III} peak with the half-wave potential ($E_{1/2}$) of +632 mV versus Ag/AgCl, similar to the reported value.[18] The value increases for **Mn-2Hyd** ($E_{1/2}$ = 754 mV) and **Mn-1CHyd** (790 mV). In comparison, **Mn-2CHyd** showed an irreversible Mn^{II}/Mn^{III} peak centered at 969 mV (E_{pa}) and a ligand oxidation peak at 731 mV, which was assigned according to

the corresponding Zn^{2+} complex. This indicates that the Mn^{2+} ion is less susceptible to oxidation in **Mn-2CHyd**. Next, we measured the longitudinal relaxivity change of the Mn^{2+} complexes in the presence of 25 equiv. Zn^{2+}. All 3 α-substituted **Mn-1,4-DO2A** derivatives were 3-fold more inert to Mn^{2+} release than the parent **Mn-1,4-DO2A** (Figure 2c).

Temperature dependence of the $H_2{}^{17}O$ transverse relaxivity[11] indicated that *q* decreased from 0.90 in **Mn-1,4-DO2A** to 0.44 in all 3 α-substituted **Mn-1,4-DO2A** derivatives (Figure 2d), which results in lower relaxivities of these α-substituted **Mn-1,4-DO2A** complexes in PBS (1.6–1.8 $mM^{-1}s^{-1}$, Figure 2e) compared to **Mn-1,4-DO2A** (2.1 $mM^{-1}s^{-1}$), even though the former have higher molecular weights which is usually associated with higher relaxivity.[22]

We then compared the reactivity of the complexes with butyraldehyde, a small-molecule model of Lys^{Ald}, by high-performance liquid chromatography in combination with inductively coupled plasma mass spectrometry (HPLC-ICP-MS). Figure 3a shows that the fastest formation of the corresponding hydrazone complex was with **Mn-2CHyd** with both conversion yield and association rate constant 2-fold higher than **Mn-1CHyd** (Figure 3b and S26) at pH 7.4. When compared to the electron rich alkyl hydrazine **Mn-2CHyd** which formed a dual hydrazone product, the electron poor acyl hydrazine bearing **Mn-2Hyd** had a lower on-rate, a slightly lower conversion yield after 90 min, and did not form the dual hydrazone product under the same reaction conditions. Interestingly the reactivity of **Mn-2Hyd** significantly increased under more acidic condition (pH 6.5, Figure S27), and suggests the potential of **Mn-2Hyd** as a pH-sensitive Lys^{Ald} targeting probe. During all the reactions no free manganese was detected, further demonstrating the stability of the complexes.

Next we examined the reaction of the Mn(II) complexes with Lys^{Ald} bearing bovine serum albumin (BSA^{Ald}) to evaluate the effect of protein-conjugation. BSA^{Ald} was prepared *via* Fe^{2+}/H_2O_2-mediated Fenton reaction with BSA. As shown in Figure 2e, in BSA, the relaxivities of all Mn(II) complexes were similar to those in PBS, indicating there was negligible non-specific binding. However, the relaxivities significantly increased in BSA^{Ald}, with 42, 37, 103% increases for **Mn-2Hyd**, **Mn-1CHyd** and **Mn-2CHyd**, respectively. We separated the BSA^{Ald} bound species by using an ultracentrifugation 5000 Da filter and quantified the binding yields and relaxivities. **Mn-2CHyd** showed the highest binding yield under various concentrations and exhibited an almost 4-fold turn-on in relaxivity when bound to BSA^{Ald} (7.7 $mM^{-1}s^{-1}$, Figure 3c–d). In comparison, the protein-bound **Mn-1CHyd** showed lower relaxivity (5.2 $mM^{-1}s^{-1}$), demonstrating the effectiveness of the dual binding approach in boosting relaxivity upon binding by restricting molecular rotation.

In vivo pharmacokinetics

As **Mn-1CHyd** and **Mn-2CHyd** showed higher reactivity and relaxivity in BSA^{Ald} than **Mn-2Hyd**, we further tested these two complexes *in vivo* and studied their pharmacokinetics in normal mice using PET-MRI. The ligands were radiolabeled with the positron emitting isotope Mn-52 (5.6 d half-life) under similar preparation conditions as for the stable Mn-55 complex (Figure S28), and then co-injected intravenously (i.v.) with nonradioactive

complex (0.1 mmol/kg) to allow PET-MR imaging, Figure 4a. Both probes underwent rapid elimination from the blood through the kidneys into the urinary bladder post injection (p.i.). However, **Mn-1CHyd** showed high liver enhancement with both MRI and PET, possibly due to increased hepatobiliary elimination arising from the hydrophobicity of the butyl chain. **Mn-2CHyd** showed little enhancement in the healthy liver over time (Figure 4a–b). At 60 mins p.i., biodistribution of manganese shows baseline Mn levels in liver with **Mn-2CHyd** but elevated levels with **Mn-1CHyd** (Figure S29). After 24 h, Mn-52 biodistribution also showed lower retention of Mn-52 from **Mn-2CHyd** in various organs compared to Mn-52 from **Mn-1CHyd** (Figure 4c). These studies indicate that **Mn-1CHyd** is unsuitable for molecular MR of liver because of the high nonspecific liver signal arising from the liver uptake of **Mn-1CHyd**.

In vivo detection of liver fibrogenesis

Because of its high stability, high turn-on in relaxivity upon binding, and low accumulation in healthy liver, we next tested whether **Mn-2CHyd** enhanced MRI could detect liver fibrogenesis *in vivo*. Mice were gavaged with CCl_4 or olive oil vehicle for 12 weeks to induce liver fibrosis. Sirius Red fibrosis staining[23] shows fibrotic liver in the CCl_4 mice. Quantification of the positive staining as collagen proportional area (CPA) was found to be 10-fold higher in the CCl_4 group *vs*. the vehicle-treated group (Figure S30). LOX is the enzyme that oxidizes Lys to Lys^{Ald} in collagens. Immunohistochemistry staining showed higher LOX immunoreactivity in the CCl_4-treated group (Figure S31). An established DNPH reactivity assay showed significantly elevated extracellular Lys^{Ald} levels in CCl_4 mice (Figure S32).[24] Liver hydroxyproline concentration, a quantitative marker of collagen,[23] also significantly increased after CCl_4 injury (Figure S33). These data confirmed the consistent fibrosis and fibrogenesis in the CCl_4 injured mice.

MRI was performed in CCl_4 and vehicle treated mice prior to and immediately following 0.1 mmol/kg i.v. administration of **Mn-2CHyd** or **Gd-DOTA** as a negative control. Figure 5a shows that at 45 mins p.i. there were no liver enhancement with **Gd-DOTA** in CCl_4 mice, but strong signal enhancement and high increase in liver-to-muscle contrast to noise ratio (ΔCNR) after **Mn-2CHyd** administration in CCl_4 treated mice. The CCl_4 treated mice imaged with **Mn-2CHyd** also showed significantly higher liver enhancement and slower liver clearance rate than the vehicle treated group (Figure 5b–c). These data indicated that **Mn-2CHyd** is highly sensitive and specific for *in vivo* detection of liver fibrogenesis. ICP-MS analysis at 75 min p.i. showed that liver Mn concentrations were approaching the endogenous Mn value in both CCl_4 and vehicle-treated mice after **Mn-2CHyd** imaging (Figure S34). Because of the high endogenous Mn liver levels, elemental analysis was not sensitive to distinguish differences in liver Mn after administration of **Mn-2CHyd** in CCl_4 versus vehicle treated mice.

CONCLUSIONS

In conclusion, rational design results in a Mn^{2+}-based MR probe that is stable to oxidation, kinetically inert to dissociation, has low signal enhancement in normal mouse liver, but strong signal enhancement in fibrogenic liver as a result of high affinity for Lys^{Ald} and

a 4-fold relaxivity turn-on upon Lys^{Ald} binding. The ability of the probe to detect liver fibrogenesis was demonstrated *in vivo*, where **Mn-2CHyd** shows significantly enhanced liver MR signal in fibrogenic mice than in healthy mice, and can detect pathology not detectable with the nonspecific clinical contrast agent **Gd-DOTA**. The Mn complexes could also be radiolabeled with ^{52}Mn and detectable by simultaneous PET-MR imaging. Here we used PET-MR to study biodistribution, but these dual modality probes could also be used for future quantitative measurements, for example to assess *in vivo* relaxivity. The data presented here enables further development and application of manganese-based hydrazine equipped probes for imaging liver fibrogenesis.

Supplementary Material

Refer to Web version on PubMed Central for supplementary material.

ACKNOWLEDGMENT

The authors acknowledge research support from the National Institute of Diabetes and Digestive and Kidney Diseases (DK121789), the National Institutes of Health Office of the Director (OD025234, OD010650, OD023503, OD028499), and the Department of Energy (DESC0021269).

Y.N. and P.C. are inventors of a filed patent application based on the work here. P.C. has equity in and is a consultant to Collagen Medical LLC, has equity in Reveal Pharmaceuticals Inc, and has research support from Pliant Therapeutics, Takeda and Janssen. The other authors have declared that no conflict of interest exists.

REFERENCES

(1). Kisseleva T; Brenner D Molecular and cellular mechanisms of liver fibrosis and its regression. Nat Rev Gastroenterol Hepatol 2021, 18 (3), 151–166. [PubMed: 33128017]

(2). Wynn TA; Ramalingam TR Mechanisms of fibrosis: therapeutic translation for fibrotic disease. Nat Med 2012, 18 (7), 1028–1040. [PubMed: 22772564]

(3). Roehlen N; Crouchet E; Baumert TF Liver Fibrosis: Mechanistic Concepts and Therapeutic Perspectives. Cells 2020, 9 (4).

(4). Patel K; Sebastiani G Limitations of non-invasive tests for assessment of liver fibrosis. JHEP Rep 2020, 2 (2), 100067. [PubMed: 32118201]

(5). Waghorn PA; Jones CM; Rotile NJ; Koerner SK; Ferreira DS; Chen HH; Probst CK; Tager AM; Caravan P Molecular Magnetic Resonance Imaging of Lung Fibrogenesis with an Oxyamine-Based Probe. Angew Chem Int Ed 2017, 56 (33), 9825–9828.

(6). Chen HH; Waghorn PA; Wei L; Tapias LF; Schuhle DT; Rotile NJ; Jones CM; Looby RJ; Zhao G; Elliott JM; et al. Molecular imaging of oxidized collagen quantifies pulmonary and hepatic fibrogenesis. JCI Insight 2017, 2 (11), e91506. [PubMed: 28570270]

(7). Kanal E Gadolinium based contrast agents (GBCA): Safety overview after 3 decades of clinical experience. Magn Reson Imaging 2016, 34 (10), 1341–1345. [PubMed: 27608608]

(8). Gupta A; Caravan P; Price WS; Platas-Iglesias C; Gale EM Applications for Transition-Metal Chemistry in Contrast-Enhanced Magnetic Resonance Imaging. Inorg Chem 2020, 59 (10), 6648–6678. [PubMed: 32367714]

(9). Zhou IY; Ramsay IA; Ay I; Pantazopoulos P; Rotile NJ; Wong A; Caravan P; Gale EM Positron Emission Tomography-Magnetic Resonance Imaging Pharmacokinetics, In Vivo Biodistribution, and Whole-Body Elimination of Mn-PyC3A. Invest Radiol 2021, 56 (4), 261–270. [PubMed: 33136686]

(10). Wahsner J; Gale EM; Rodriguez-Rodriguez A; Caravan P Chemistry of MRI Contrast Agents: Current Challenges and New Frontiers. Chem Rev 2019, 119 (2), 957–1057. [PubMed: 30350585]

(11). Gale EM; Atanasova IP; Blasi F; Ay I; Caravan P A Manganese Alternative to Gadolinium for MRI Contrast. J Am Chem Soc 2015, 137 (49), 15548–15557. [PubMed: 26588204]

(12). Ndiaye D; Sy M; Pallier A; Meme S; de Silva I; Lacerda S; Nonat AM; Charbonniere LJ; Toth E Unprecedented Kinetic Inertness for a Mn^{2+}-Bispidine Chelate: A Novel Structural Entry for Mn^{2+}-Based Imaging Agents. Angew Chem Int Ed 2020, 59 (29), 11958–11963.

(13). Anbu S; Hoffmann SHL; Carniato F; Kenning L; Price TW; Prior TJ; Botta M; Martins AF; Stasiuk GJ A Single-Pot Template Reaction Towards a Manganese-Based T1 Contrast Agent. Angew Chem Int Ed 2021, 60 (19), 10736–10744.

(14). Botar R; Molnar E; Trencsenyi G; Kiss J; Kalman FK; Tircso G Stable and Inert Mn(II)-Based and pH-Responsive Contrast Agents. J Am Chem Soc 2020, 142 (4), 1662–1666. [PubMed: 31927927]

(15). Barandov A; Bartelle BB; Williamson CG; Loucks ES; Lippard SJ; Jasanoff A Sensing intracellular calcium ions using a manganese-based MRI contrast agent. Nat Commun 2019, 10 (1), 897. [PubMed: 30796208]

(16). Davies G; Kustin K Stoichiometry and kinetics of manganese (III) reactions with hydrazine and the methylhydrazines in acid perchlorate solution. J. Phys. Chem 1969, 73 (7), 2248–2253.

(17). Rolla GA; Platas-Iglesias C; Botta M; Tei L; Helm L ^{1}H and ^{17}O NMR relaxometric and computational study on macrocyclic Mn(II) complexes. Inorg Chem 2013, 52 (6), 3268–3279. [PubMed: 23437979]

(18). Garda Z; Forgacs A; Do QN; Kalman FK; Timari S; Baranyai Z; Tei L; Toth I; Kovacs Z; Tircso G Physico-chemical properties of Mn(II) complexes formed with *cis*- and *trans*-DO2A: thermodynamic, electrochemical and kinetic studies. J Inorg Biochem 2016, 163, 206–213. [PubMed: 27567150]

(19). Zhang Z; Greenfield MT; Spiller M; McMurry TJ; Lauffer RB; Caravan P Multilocus binding increases the relaxivity of protein-bound MRI contrast agents. Angew Chem Int Ed 2005, 44 (41), 6766–6769.

(20). Kielar F; Tei L; Terreno E; Botta M Large Relaxivity Enhancement of Paramagnetic Lipid Nanoparticles by Restricting the Local Motions of the Gd^{III} Chelates. J. Am. Chem. Soc 2010, 132, 7836–7837. [PubMed: 20481537]

(21). Akam EA; Abston E; Rotile NJ; Slattery HR; Zhou IY; Lanuti M; Caravan P Improving the reactivity of hydrazine-bearing MRI probes for in vivo imaging of lung fibrogenesis. Chem Sci 2020, 11 (1), 224–231. [PubMed: 32728411]

(22). Helm L; Morrow JR; Bond CJ; Carniato F; Botta M; Braun M; Baranyai Z; Pujales-Paradela RR-F,M; Esteban-Gomez D; Platas-Iglesias C; et al. In Contrast Agents for MRI: Experimental Methods, The Royal Society of Chemistry, 2017; pp 121–242.

(23). Standish RA; Cholongitas E; Dhillon A; Burroughs AK; Dhillon AP An appraisal of the histopathological assessment of liver fibrosis. Gut 2006, 55 (4), 569–578. [PubMed: 16531536]

(24). Zhong Y; Mahoney RC; Khatun Z; Chen HH; Nguyen CT; Caravan P; Roberts JD Jr. Lysyl oxidase regulation and protein aldehydes in the injured newborn lung. Am J Physiol Lung Cell Mol Physiol 2022, 322 (2), L204–L223. [PubMed: 34878944]

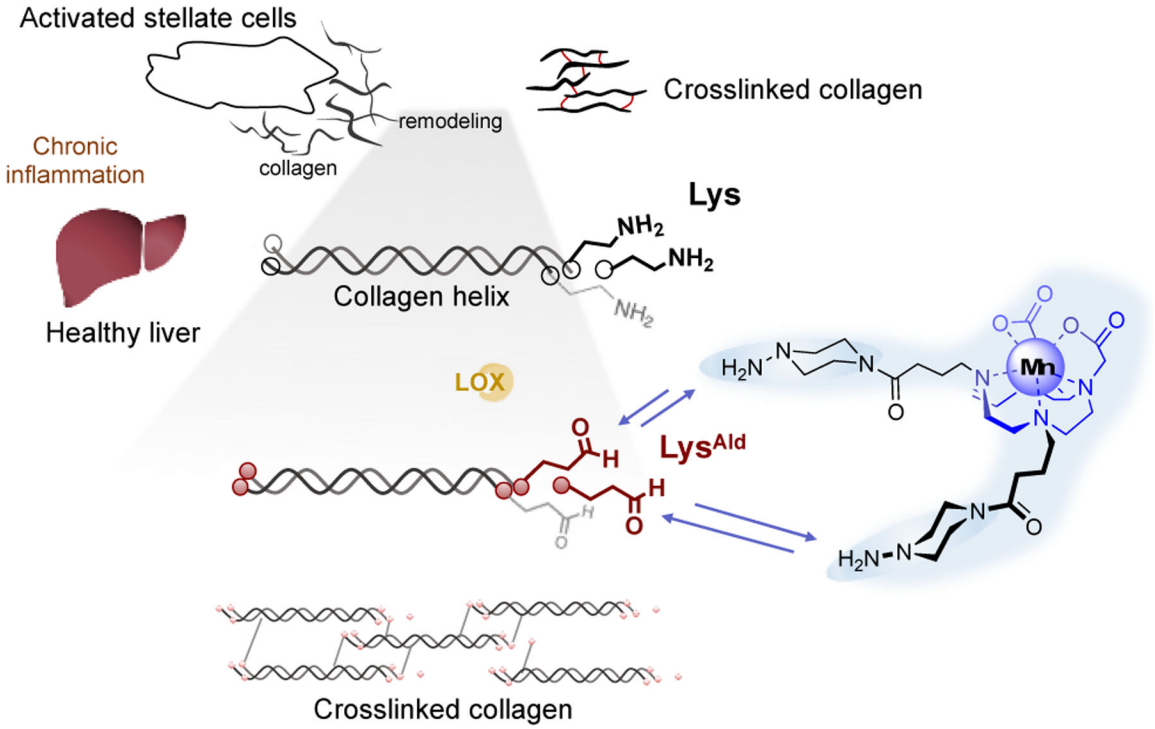

Figure 1.

Schematic illustration of the design of a reversible and dual binding Mn^{2+} probes for targeting Lys^{Ald} residues in the process of liver fibrogenesis.

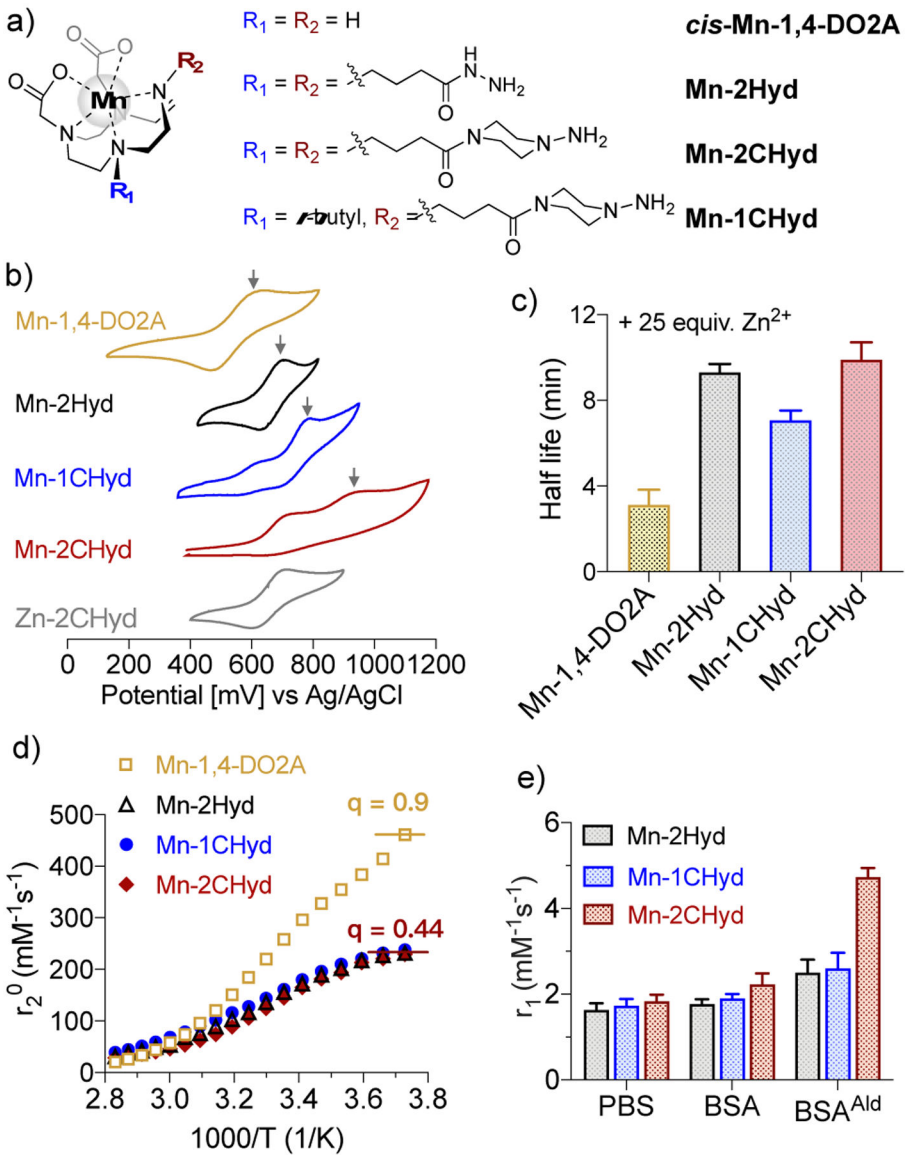

Figure 2.

a) Chemical structures of the Mn(II) complexes studied here; b) Cyclic voltammograms of the complexes in H_2O containing 0.1 M KNO_3 (pH 6.5, mV vs Ag/AgCl, arrows mark the Mn^{II}/Mn^{III} peak); c) Half-life of 1 mM Mn(II) complexes upon challenge with 25 mM Zn^{2+} monitored by longitudinal relaxivity in 50 mM pH 6.0 MES buffer, 37 °C, 1.41 T; d) $H_2{}^{17}O$ transverse relaxivity in the presence of corresponding Mn^{2+} complex as a function of temperature. Peak relaxivity is indicative of the number of inner-sphere water molecules (*q*); e) Relaxivity values in PBS alone or with 10 mg/mL BSA or BSA^{Ald} (pH 7.4, 2 h incubation, 37 °C, 1.41 T).

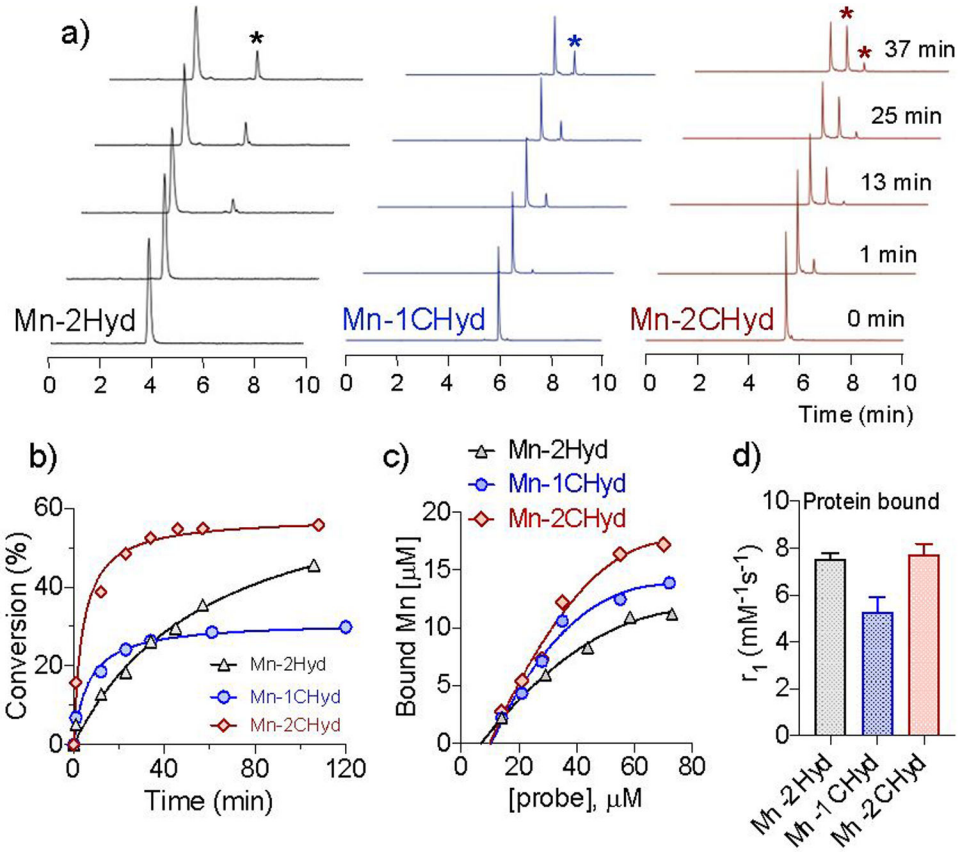

Figure 3.

a) Time course HPLC-ICP-MS trace of Mn(II) complexes (25 μM) in the presence of 100 μM butyraldehyde (PBS, pH 7.4, rt, stars mark the hydrazone products); b) Conversion yield versus time of corresponding Mn(II) complex in a); c) Concentration of BSA^{Ald} bound Mn(II) complex under different concentrations (10 mg/mL BSA^{Ald}, pH 7.4, 2 h incubation, 37°C); d) Relaxivity of BSA^{Ald} bound Mn species (PBS, pH 7.4, 2 h incubation, 37°C, 1.41 T).

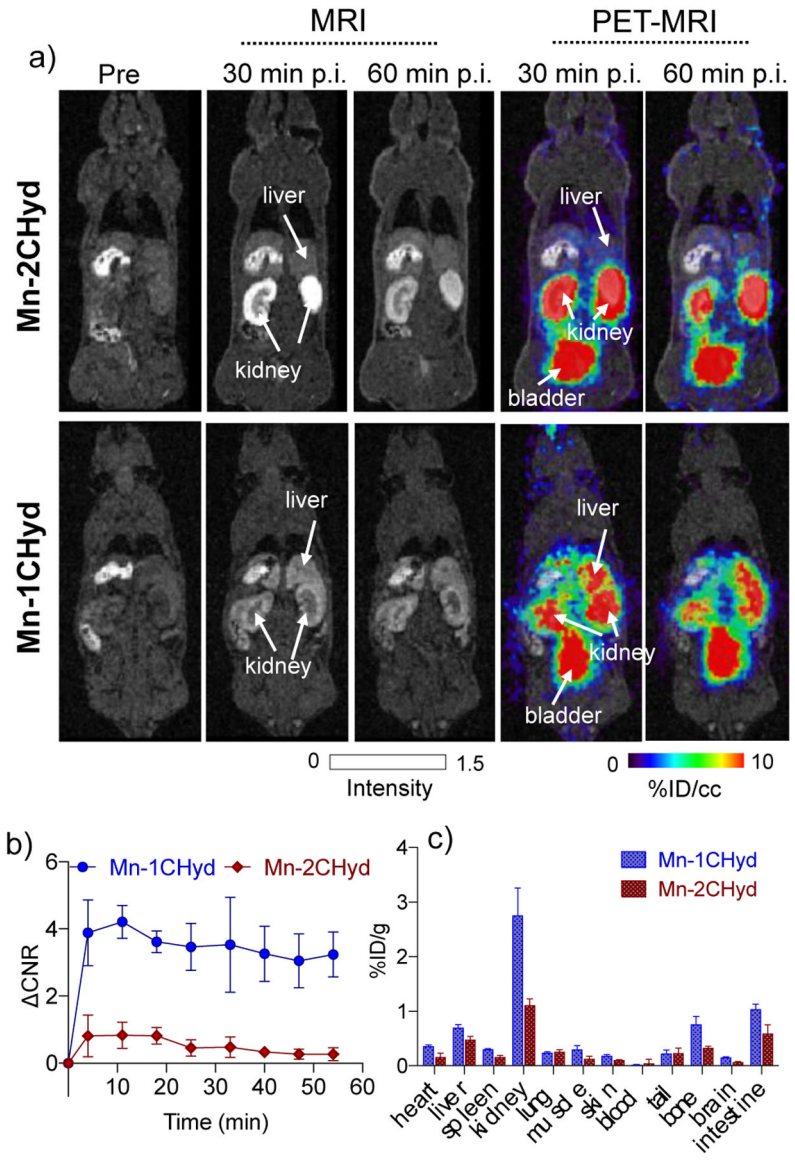

Figure 4.

a) Whole body MRI (grey scale) and PET-MRI (color scale) images of normal mice imaged at pre-, 30- and 60 mins post-injection of 0.1 mmol/kg [^{52}Mn]**Mn-2CHyd** or [^{52}Mn]**Mn-1CHyd**. PET imaging is reported as percent injected dose per cubic centimeter (% ID/cc); b) Change in liver to muscle MRI contrast to noise ratio (ΔCNR) over time for **Mn-2CHyd** or **Mn-1CHyd** in normal mice (n = 6); c) *Ex vivo* biodistribution of Mn-52 at 24 h p.i. of **Mn-2CHyd** or **Mn-1CHyd**, expressed as percent injected dose per gram of tissue (%ID/g) (mean ± SD) in various organs (n = 3).

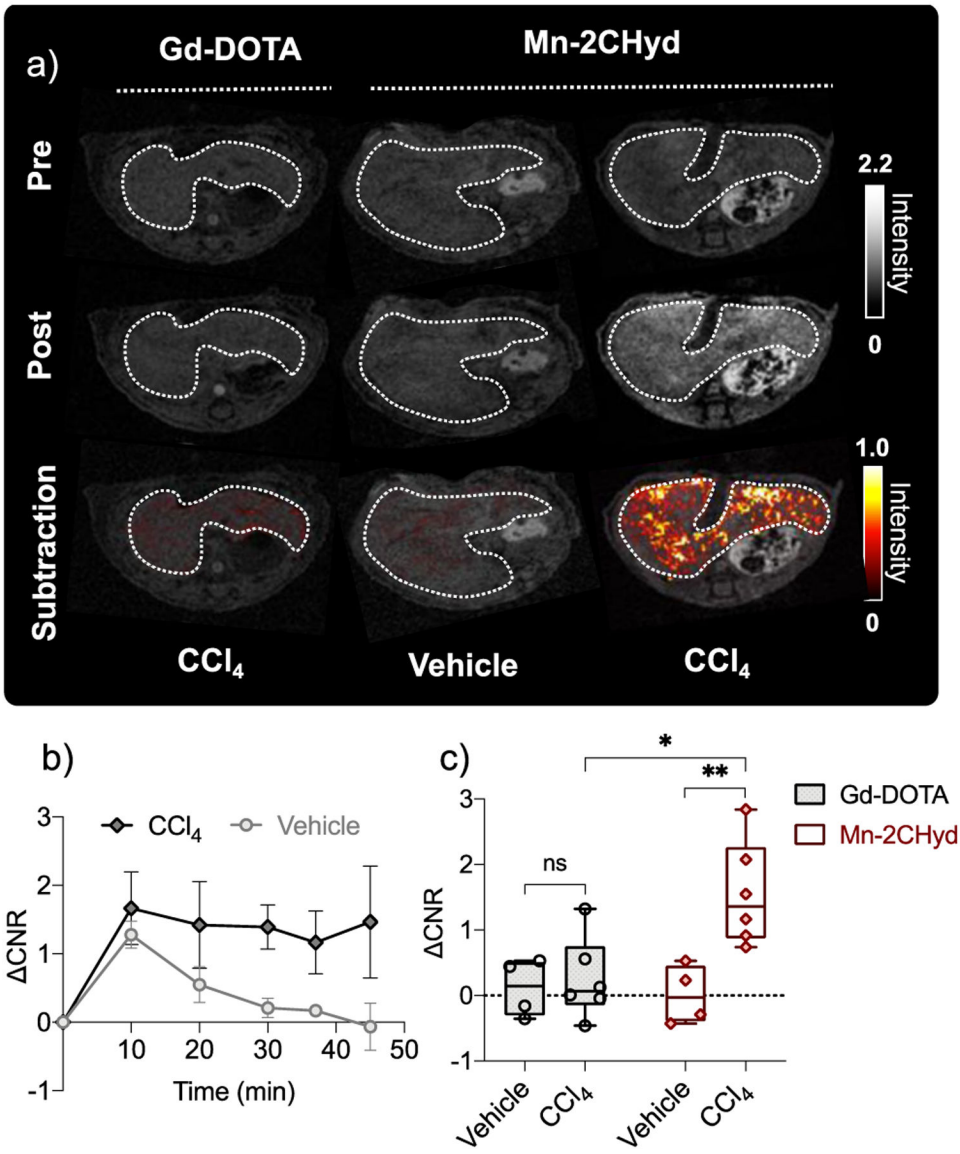

Figure 5.

a) Axial liver (outlined in dotted white lines) images of CCl_4 and vehicle treated mice imaged before (pre) and 45 min p.i. (post) of **Gd-DOTA** or **Mn-2CHyd** (0.1 mmol/kg i.v., grey scale), and corresponding post-pre subtraction liver images (color scale); b) Post-pre change in liver to muscle contrast to noise ratio (ΔCNR) change over time for CCl_4 and vehicle treated mice imaged with **Mn-2CHyd**; c) ΔCNR in vehicle treated (n = 4) and CCl_4 mice (n = 6) at 45 mins p.i. of **Gd-DOTA** and **Mn-2CHyd**. *$P < 0.05$, **$P < 0.01$, ns, not significant, unpaired student t test.